Temperature sensing by means of a near-infrared luminescent $Ca_8NaBi(PO_4)_6F_2:Nd^{3+}$ fluorapatite phosphor

Abir Douzi[1,2], Sami Slimi[1], Pavel Loiko[3], Victor Llamas[4], Josep María Serres[5], Rosa Maria Solé[1], Magdalena Aguiló[1], Francesc Díaz[1], Ezzedine Ben Salem[2], and Xavier Mateos[1,5,*]

[1] *Universitat Rovira I Virgili (URV), Física i Cristal·Lografia de Materials (FiCMA), Marcel·li Domingo 1, 43007 Tarragona, Spain*

[2] *I.P.E.I. of Monastir, Unit of Materials and Organic Synthesis UR17ES31, University of Monastir, 5019 Monastir, Tunisia*

[3] *Centre de Recherche sur Les Ions, Les Matériaux et La Photonique (CIMAP), UMR 6252 CEA-CNRS-ENSICAEN, Université de Caen Normandie, 6 Boulevard Maréchal Juin, 14050 Caen Cedex 4, France*

[4] *Advanced Manufacturing Systems Unit (AMS), Centre Tecnològic de Catalunya, Marcel·lí Domingo 2, 43007 Tarragona, Spain*

[5] *Serra Húnter Fellow, Reus, Spain*

ABSTRACT

Microrods of calcium sodium bismuth fluorapatite doped with neodymium, denoted as $Ca_8NaBi_{1-x}Nd_x(PO_4)_6F_2$ (with x ranging from 0 to 0.5), were synthetized using a modified Pechini sol–gel method. The crystalline structure of these phosphors was refined using the Rietveld method and exhibited hexagonal symmetry with space group $P6_3/m - C^2_{6h}$, where the lattice parameters were $a = 9.3855(5)$ Å and $c = 6.8998(6)$ Å for $x = 0.2$. The particles morphology was analyzed through SEM, revealing an average length of approximately 1.5 μm. When excited at 808 nm, the $Ca_8NaBi(PO_4)_6F_2:0.2Nd^{3+}$ microrods emitted strongly at 872, 957 and 1055 nm, falling within the near-infrared region. These emissions correspond to the $^4F_{3/2} \rightarrow ^4I_{9/2}$ (P2), $^4F_{5/2} \rightarrow ^4I_{11/2}$ (P3), $^4F_{3/2} \rightarrow ^4I_{11/2}$ (P1) transitions of Nd^{3+} ions, respectively, and are situated within the first and second biological windows. The luminescence lifetime of the $^4F_{3/2}$ state of Nd^{3+} was measured to be 294.4 μs for the sample with the lowest Nd^{3+} concentration of $x = 0.05$. In addition, the luminescence intensity ratios P2/P1 and P3/P1 were found to be temperature dependent, potentially making it suitable for luminescent ratiometric thermal sensing. These findings suggest that the synthesized $Ca_8NaBi(PO_4)_6F_2:Nd^{3+}$ microrod thermometers exhibit favorable characteristics in terms of relative sensitivity, temperature uncertainty, and repeatability within the temperature range of 303–403 K.

Address correspondence to E-mail: xavier.mateos@urv.cat

Springer

1 Introduction

Fluorescence intensity ratio (FIR) optical thermometry using rare-earth (RE)-doped materials has gained significant importance, particularly due to the distinctive fluorescence emission exhibited by these elements within the visible and near-infrared (NIR) spectral range [1–5]. This approach has benefited from thorough investigations into luminescent materials. Initial research primarily concentrated on utilizing thermographic phosphors in areas such as aerodynamics, high-speed wind tunnels, gas turbine engines, electrical transformer networks, clinical diagnostics, high-speed integrated circuits, and advanced fiber thermometry systems [6–12]. More recent progress in nanotechnology has given rise to luminescence micro and nanothermometry, driven by the growing demand for precise temperature determination on smaller scales, particularly for practical applications in micro/nanoelectronics, embedded photonics, metallurgy, catalysis, and high-pressure chambers [4, 13].

Luminescent thermometry primarily relies on examining temperature-induced changes in spectral properties, including intensity, spectral position, band shape, lifetime, and polarization [14]. The FIR method hinges on the ratio of fluorescence intensity of two emission lines affected by temperature. This technique has garnered significant attention due to its innate resilience to certain external disturbances during the detection process, such as loss of fluorescence, the quantity of phosphors, and variations in excitation intensity [15]. Phosphors that undergo both down- and up-conversion and are doped with various rare-earth ions like Nd^{3+}, Dy^{3+}, Ho^{3+}, Er^{3+}, Tm^{3+}, and Eu^{3+} have proven to be effective as FIR based-thermal sensors [16–21]. The neodymium ion, denoted as Nd^{3+}, which exhibits absorption around 800 nm, is considered a promising choice for achieving efficient emission in the first biological window (I-BW) spanning from 700 to 950 nm, as well as in the second biological window (II-BW) extending from 1000 to 1400 nm. This efficiency is based on the three primary emission pathways of Nd^{3+}: $^4F_{3/2} \rightarrow {}^4I_{9/2}$, $^4F_{3/2} \rightarrow {}^4I_{11/2}$, and $^4F_{3/2} \rightarrow {}^4I_{13/2}$, resulting in emissions at approximately 910 nm, 1050 nm, and 1330 nm, respectively. In the context of Nd^{3+} ions, there are two established methods for monitoring temperature variations. The first approach involves analyzing the emission bands associated with transitions between the Stark sub-levels of $^4F_{3/2}$ (Ri) and $^4I_{9/2}$ (Xj) or $^4I_{11/2}$ (Yk) levels. However,

this method has inherent limitations, including relatively low relative sensitivity (around 0.1% K^{-1}) and a narrow thermal detection range due to the small energy gap between the two Stark components (typically about 100 cm^{-1}). An alternative method relies on the ratio of luminescence intensity for the $^4F_{5/2} \rightarrow {}^4I_{9/2}$ and $^4F_{3/2} \rightarrow {}^4I_{9/2}$ transitions. This approach was initially introduced for thermal sensing within the biophysical temperature range by Balabhadra et al. [23]. It was observed that a greater energy difference between the excited levels led to a significant improvement in thermal sensitivity.

To date, a range of inorganic nanoparticles activated by Nd^{3+} ions have been successfully synthesized and have quickly found exciting applications in luminescence nanothermometry. These nanoparticles encompass various materials, including Nd^{3+}-doped fluorides like $LaF_3:Nd^{3+}$ [24], $CaF_2:Nd^{3+}$ [25], garnets such as $Y_3Al_5O_{12}:Nd^{3+}$ [26], and vanadates like $YVO_4:Nd^{3+}$ [27] and $BiVO_4:Nd^{3+}$ [28]. It is important to note that the thermal sensitivity of these systems can vary, depending on the magnitude of thermally induced spectral changes. Consequently, optimizing the crystalline structure is often employed to enhance the sensitivity of thermometers based on Nd^{3+}. However, it is worth emphasizing that the development of highly sensitive Nd^{3+}-doped luminescent nanoparticles with a narrow size distribution, consistent morphology, and excellent colloidal stability remains a pressing priority for applications in the biological field [29].

Due to their strong chemical stability and well-defined crystalline structure, apatite compounds $L_{10}(XO_4)_6Y_2$ (where L = Ca, Sr, Ba, La, Y, X = P, V, Si, and Y = F, Cl, Br, OH), which crystallize in the hexagonal system with the $P6_3/m$ space group, have been extensively explored as exceptional materials for hosting luminescent properties [30]. Apatite materials, like fluorapatite, are well-known synthetic bioceramics recognized for their remarkable biocompatibility, stemming from their similarity to the inorganic tissue present in the bone matrix [31]. Among these apatite compounds, calcium sodium bismuth fluorapatite, $Ca_8NaBi(PO_4)_6F_2$, has been recognized as an excellent host for incorporating Eu^{3+} ions [32]. However, up to this point, there has not been any exploration of the application of Nd^{3+}-activated $Ca_8NaBi(PO_4)_6F_2$ phosphors for optical thermometry.

In the present work, Nd^{3+}-doped $Ca_8NaBi(PO_4)_6F_2$ microrods have been successfully synthesized by a modified Pechini method. The crystalline structure,

size, and morphology of the as-prepared phosphors were examined. The effect of the Nd^{3+} doping concentration on the luminescence spectra and lifetimes was investigated. In addition, we carried out an in-depth investigation of the photoluminescence behavior at different temperatures for these fabricated microrods, aiming to design innovative luminescent thermometers.
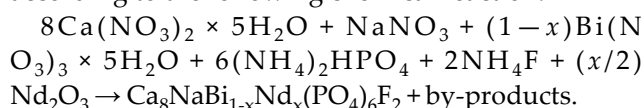
2 Experimental section

2.1 Synthesis of nanorods

The compounds with a chemical formula $Ca_8NaBi_{1-x}Nd_x(PO_4)_6F_2$, both undoped ($x = 0$) and doped with Nd^{3+} ions at several concentrations of $x = 0.05, 0.1, 0.2, 0.3, 0.4$, and 0.5 were prepared using the modified Pechini method. First, $Ca(NO_3)_2 \times 5H_2O$ (Alfa Aesar, 99.0%), $NaNO_3$, and $Bi(NO_3)_3 \times 5H_2O$ (Aldrich, 99.5%) in stoichiometric amounts were dissolved in distilled water. Nd_2O_3 (Aldrich, 99.9%) was dissolved in nitric acid (Labkem, 65%) to obtain the nitrated form of Nd. The procedure began with the addition of neodymium nitrate solution to the previously mentioned aqueous solution. Simultaneously, a citric acid (CA) solution was introduced as a chelating agent to form a transparent solution. These solutions were mixed, and ethylene glycol (EG) was included as a surfactant to initiate esterification. The solution composed of $(NH_4)_2HPO_4$ and NH_4F was then gradually added drop by drop to the cation-citrate complex. The molar ratio of metals to CA to EG was maintained at 1:2:2. The entire reagent mixture underwent stirring and heating simultaneously, reaching 80 °C to achieve a gel-like consistency. The product's viscosity progressively increased until it transformed into a resinous gel. This phase was considered complete when

a whitish gel was visible at the bottom of the crucible. At this point, the stirring device was removed. The resulting resin was subsequently heated to 120 °C to yield the dried precursor. Finally, the obtained precursor powder was subjected to calcination at 900 °C for a duration of 10 h and then allowed to cool to room temperature. The synthesis of a series of $Ca_8NaBi(PO_4)_6F_2$:xNd^{3+} phosphors followed the procedure outlined in Fig. 1.

The synthesis of these phosphors was performed according to the following chemical reaction:

$$8Ca(NO_3)_2 \times 5H_2O + NaNO_3 + (1-x)Bi(NO_3)_3 \times 5H_2O + 6(NH_4)_2HPO_4 + 2NH_4F + (x/2)Nd_2O_3 \rightarrow Ca_8NaBi_{1-x}Nd_x(PO_4)_6F_2 + by\text{-}products.$$

3 Characterization techniques

The XRD measurements were carried out in a θ-θ Bragg–Brentano configuration, utilizing a Bruker-AXS D8-Advance diffractometer fitted with a PSD Lynx-Eye detector featuring an opening angle of 2.94º and Cu Kα (1.5406 Å) radiation. To refine the crystalline structure, XRD patterns were recorded within a 2θ range spanning from 10° to 70°, employing a step time of 2s and a step size of 0.02°. Raman spectra were acquired using a Renishaw InVia confocal Raman microscope, which included an edge filter, a Leica × 50 objective, and an Ar$^+$ ion laser as the excitation source (514 nm). Furthermore, infrared (IR) absorption spectra were collected through a Fourier transform infrared spectrometer (FTIR, model FI/IR 6700, Jasco). For the examination of the synthesized powders' morphology, a JEOL 1011 scanning electron microscope (SEM) was employed. To ascertain their chemical composition, electron-dispersive X-ray spectroscopy (EDS) analysis was conducted utilizing an environmental scanning electron microscope (ESEM,

Fig. 1 Illustration depicting the modified Pechini synthesis of the $Ca_8NaBi(PO_4)_6F_2$:xNd^{3+} phosphors
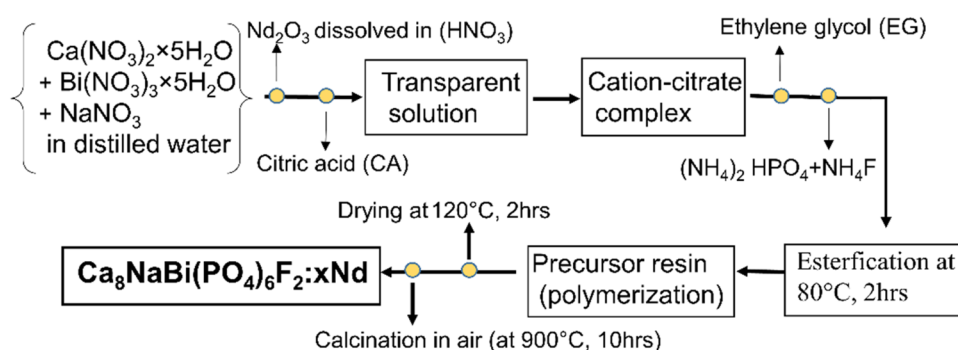
FEI Quanta 600 model) equipped with an Oxford Inca 3.0 microanalyzer.

The reflectance spectra were acquired at room temperature (RT) using a Varian CARY 5000 spectrophotometer. Measurements were taken in the range of 250–850 nm with samples in pellet form, each having a diameter of 12 mm. The spectral resolution was set at 0.5 nm. For room-temperature luminescence spectra, an AlGaAs diode laser (Ostech) emitting at 808 nm with a power up to 15 W served as the excitation source, coupled with an optical spectrum analyzer (OSA Yokogawa Electric, AQ6374E). The excitation spectra and decay curves were analyzed using an Edinburgh FLS1000 spectrofluorometer equipped with a 400 W continuous-wave xenon lamp and an 808 nm NIR laser diode for excitation. To assess the variation in luminescent properties of the $Ca_8NaBi(PO_4)_6F_2:Nd^{3+}$ micropowders with temperature, they were placed in a Linkam THMS600 heating stage, and their emission was collected in a 90° geometry to minimize the impact of pump radiation on the recorded spectra.

4 Results and discussion

4.1 Crystal structure and phase identification

The phase purity and structure of the synthesized powders, both those without doping and those doped with varying concentrations of Nd^{3+} (0.05, 0.1, 0.2, 0.3, 0.4, and 0.5 Nd^{3+}), were assessed through room-temperature powder X-ray diffraction (XRD). The obtained XRD patterns are displayed in Fig. 2a. The well-defined diffraction peaks in these diffractograms indicate the excellent crystalline quality of the synthesized materials. Notably, there are no discernible peaks in the XRD patterns that correspond to potential impurities or secondary phases, particularly free neodymium nitrate. The indexed XRD patterns confirm the presence of a single crystalline phase with hexagonal symmetry (space group: $P6_3/m—C^2_{6h}$, No. 176), consistent with the JCPDS (Joint Committee on Powder Diffraction Standards) PDF card No. 96-900-1879 for $Ca_5(PO_4)_3F$ fluorapatite, as illustrated in Fig. 2b. It is worth noting that the incorporation of Nd^{3+} doping into the host material does not bring any changes to its symmetry structure ensuring that the fundamental atomic arrangement of apatite structure and the space group configuration of the phosphor host $Ca_8NaBi(PO_4)_6F_2$ remain consistent.

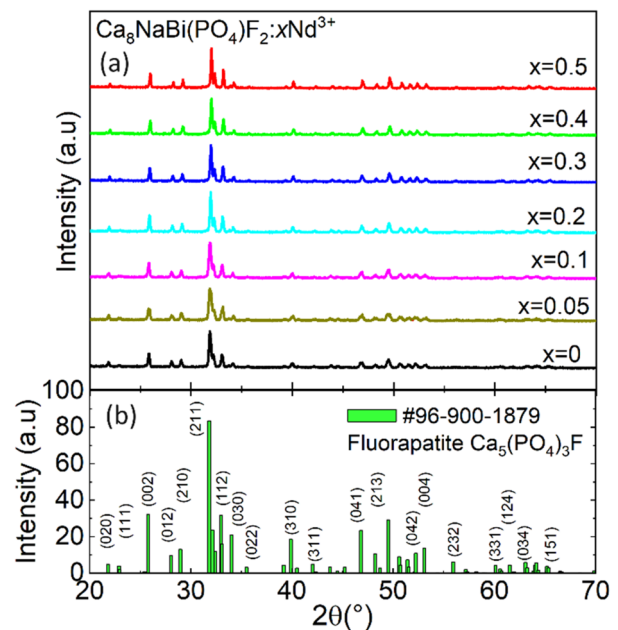**Fig. 2 a** X-ray powder diffraction (XRD) patterns of the $Ca_8NaBi(PO_4)_6F_2:xNd^{3+}$ phosphors with $x = 0$, 0.05, 0.1, 0.2, 0.3, 0.4, and 0.5; **b** theoretical pattern for fluorapatite, JCPDS card # 96-900-1879

The crystalline structure analysis was conducted through the Rietveld refinement using match!3 software. This aimed to determine the crystalline structure of the resulting powders and identify the specific sites where Nd^{3+} ions were incorporated in the host matrix. Table 1 provides a summary of the refinement parameters for the $Ca_8NaBi(PO_4)_6F_2:0.2Nd^{3+}$ sample. The determined lattice parameters were found to be $a = b = 9.3855(5)$ Å, $c = 6.8998(6)$ Å, and the unit-cell volume $V = 526.15$ Å^3. The quality of the refinement was confirmed by the reliability factors: $R_{wp} = 11.1$, $R_{exp} = 8.55$, and a chi-squared factor χ^2 of 1.69. The persistence of the hexagonal phase in Nd^{3+}-doped samples was confirmed. In Fig. 3a, a close match between the observed (Y_{obs}) and calculated (Y_{calc}) patterns is evident, underscoring the validity of the Rietveld refinement, as indicated by the minimal fit residuals ($Y_{obs}−Y_{calc}$). Based on the effective ionic radii and charge balance of cations with different coordination numbers (C.N.), it is inferred that the Nd^{3+} ions, as dopants, are likely to randomly occupy the Bi^{3+} sites in the prepared samples. This inference is supported by the close proximity of the effective ionic radii of Nd^{3+} ($R_{Nd} = 0.983$ Å for C.N. = VII and 1.163 Å for C.N. = IX) to those of Bi^{3+} ($R_{Bi} = 1.03$ Å and 1.17 Å, respectively), as compared to those of Ca^{2+} ($R_{Ca} = 1.06$ Å and 1.18 Å,

Table 1 Rietveld refinement parameters for $Ca_8NaBi(PO_4)_6F_2{:}0.2Nd^{3+}$

Parameter	Value
Chemical formula	$Ca_8NaBi_{0.8}Nd_{0.2}(PO_4)_6F_2$
Crystal class	Hexagonal
Space group	$P6_3/m$
Laue class	$6/m$
Hall symbol	-P6c
Reduced number of S.O	6
$a=b$ (Å)	9.3855(5)
c (Å)	6.8998(6)
$\alpha=\beta$	90°
γ	120°
V (Å³)	526.15
Range of 2θ	10–70
Radiation	Cu Kα (1.5406 Å)
R-factors	$R_p=8.50$, $R_{wp}=11.1$, $R_{exp}=8.55$, $\chi^2=1.69$, $R_b=1.98$

respectively) [33]. As anticipated, the substitution of Bi^{3+} by Nd^{3+} leads to a modification in the lattice parameters, specifically a reduction in the lattice constants. The lattice parameters of the non-doped host matrix were a = 9.3980(6) Å and c = 6.9039(9) Å [32].

The substitution of the host-forming (h) cations with the dopant (d) ones can be quantified by the percent difference in ionic radii ($Dr = [(Rh-Rd)/Rh] \times 100\%$). This value should not exceed 30% to maintain lattice stability [34]. In this instance, we have Rh = R_{Bi} and Rd = R_{Nd}, resulting in $Dr = 4.56\%$ for C.N. = VII and $Dr = 0.60\%$ for C.N. = IX, which comfortably meets the aforementioned criterion.

Table 2 provides details on the fractional atomic coordinates (x/a, y/b, and z/c), site occupancy factors, and isotropic displacement parameters (B_{iso}) for the $Ca_8NaBi(PO_4)_6F_2{:}0.2Nd^{3+}$ sample. The Nd^{3+} ions occupy positions 4f and 6 h in the Wyckoff scheme. Figure 3b displays a projection of the crystalline
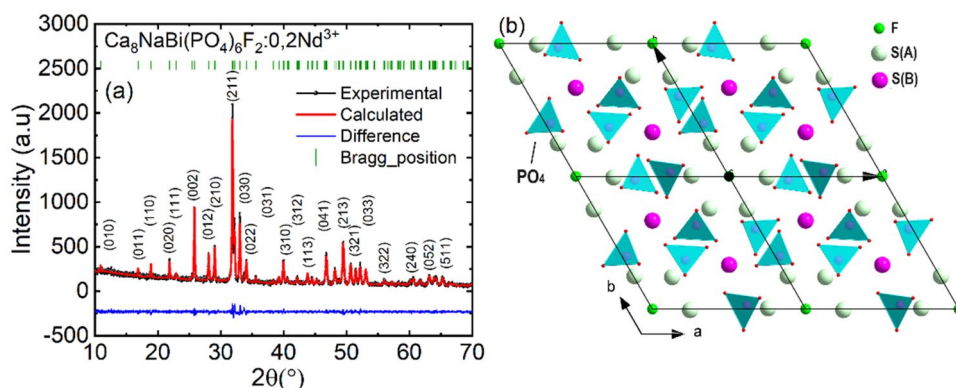

Fig. 3 a Rietveld refinement of the XRD pattern of the sample $Ca_8NaBi(PO_4)_6F_2{:}0.2Nd^{3+}$; experimental (*black*), calculated (*red*), and differential (*blue*) profiles and Bragg reflections (*green dashes*), (*hkl*) are the Miller's indices; **b** projection of the crystalline structure of $Ca_8NaBi(PO_4)_6F_2{:}Nd$ on the ***a-b*** plane

Table 2 Fractional atomic coordinates (x/a, y/b, z/c), site occupancy factors (O.F.) and isotropic displacement parameters (B_{iso}) for $Ca_8NaBi(PO_4)_6F_2{:}0.2Nd^{3+}$

Atoms	Wyckoff	x/a	y/b	z/c	O.F	B_{iso} (Å²)
Ca1	4f	0.6666 (5)	0.3335 (1)	0.0050 (9)	0.75	1.123 (3)
Ca2	6 h	0.7025 (2)	0.0085 (5)	0.2575 (3)	0.85	0.955 (7)
Na	4f	0.6666 (2)	0.3335 (6)	0.0050 (9)	0.13	1.123 (3)
Bi1|Nd1	4f	0.6666 (5)	0.3335 (1)	0.0050 (9)	0.10|0.02	1.123 (3)
Bi2|Nd2	6 h	0.7025 (2)	0.0085 (5)	0.2575 (3)	0.12|0.03	0.955 (7)
P1	6 h	0.3689 (5)	0.3885 (5)	0.2500 (0)	1.00	0.992 (0)
O1	6 h	0.4859 (4)	0.3173 (4)	0.2500 (0)	1.00	1.135 (0)
O2	6 h	0.4698 (4)	0.5901 (1)	0.2500 (0)	1.00	1.452 (5)
O3	12i	0.2601 (5)	0.3541 (3)	0.0915 (2)	1.00	1.198 (2)
F	2a	0	0	0.2500 (0)	1.00	0.715 (0)

structure of $Ca_8NaBi(PO_4)_6F_2$:Nd onto the a–b crystallographic plane, derived from the refined atomic coordinates. The structure encompasses two types of cationic sites denoted as S(A) and S(B). The S(A) site accommodates Na^+, Ca^{2+}, and Bi^{3+} cations, while the S(B) site of the other Ca^{2+} and Bi^{3+} ions. The S(A) sites exhibit point-symmetric positions in column C_3 with IX-fold oxygen coordination, while the S(A) sites are located at point-symmetric C_S triangular positions with VII-fold coordination, including one fluorine anion and six oxygen atoms.

4.2 Raman and IR spectroscopy

The Raman spectra for $Ca_8NaBi(PO_4)_6F_2$:xNd ($x = 0$, 0.1, 0.3, and 0.5) samples within the 100–1500 cm^{-1} range are illustrated in Fig. 4a. In the high-frequency region, two prominent bands at 1038 and 1080 cm^{-1} are evident, and they are attributed to the asymmetric stretching of P–O bonds (v_3). The most intense Raman peak at 961 cm^{-1} corresponds to the symmetric stretching of the P–O bonds (v1). Bands in the range of 587–614 cm^{-1}, displaying intermediate intensity, are linked to the asymmetric stretching of O–P–O bonds (v_4). In addition, the band at 436 cm^{-1} is associated with the symmetric bending of the O–P–O bonds (v_2). Lastly, bands below 300 cm^{-1} represent external modes. The Raman modes in $Ca_8NaBi(PO_4)_6F_2$:Nd were assigned based on Ref.[35]. Moving to the IR spectra of the $Ca_8NaBi(PO_4)_6F_2$:xNd^{3+} powders, Fig. 4b presents the data within the range of 400–1700 cm^{-1}. The bands spanning from 400 to 1200 cm^{-1} are attributed to the characteristic vibrations of phosphate tetrahedral groups (PO_4^{3-}). Notably, there are no significant distinctions observed in the IR spectra among the samples with x = 0, 0.1, 0.3, and 0.5. Specifically, the vibrational band at 563–603 cm^{-1} (v_4) pertains to the O–P–O bending modes, while the bands at 931 cm^{-1} (v_1) and 1024 cm^{-1} (v_3) correspond to the symmetric stretching mode of the P–O bonds.

Fig. 4 **a** Raman and **b** IR spectra of the $Ca_8NaBi(PO_4)_6F_2$:xNd samples for $x = 0$, 0.1, 0.3, and 0.5

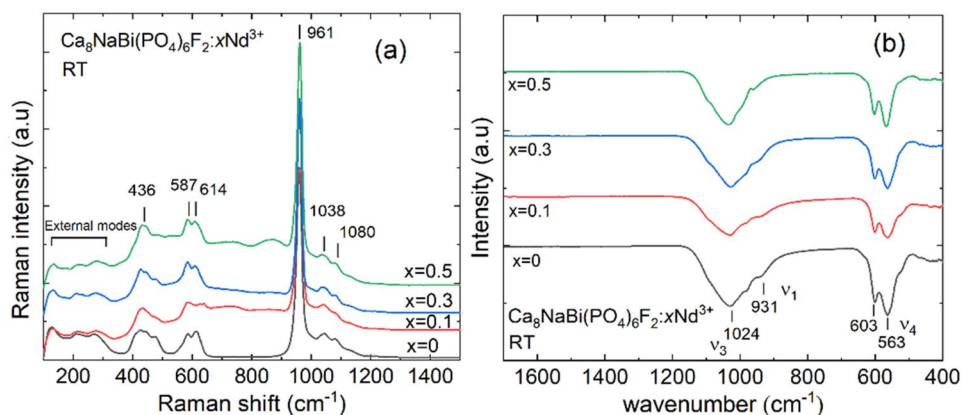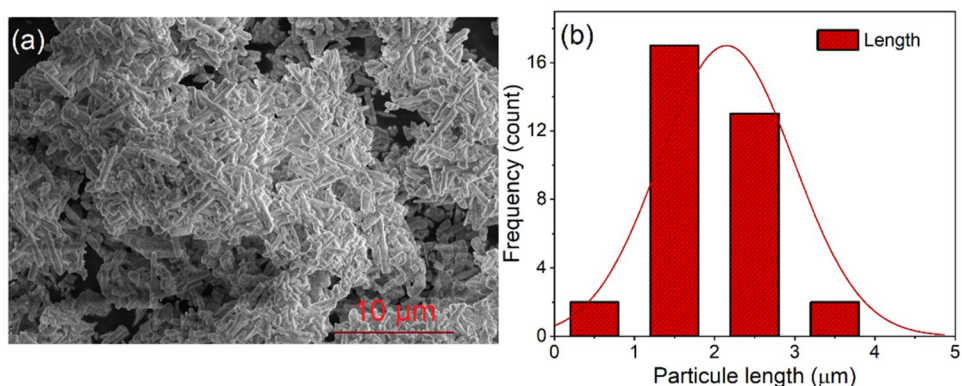**Fig. 5** **a** A typical SEM image and **b** the corresponding particle size distribution for the $Ca_8NaBi(PO_4)_6F_2$:0.2Nd phosphor

4.3 Morphology and composition of powders

Figure 5a shows a typical SEM micrograph of the $Ca_8NaBi(PO_4)_6F_2$:$0.2Nd^{3+}$ powder. It reveals particles which are about a few μm in length by one μm in width. The particles are rod shaped, which is in agreement with the previous reports on apatites [36]. They tend to grow and agglomerate to form large aggregates of rods that can exceed 10 μm in size. The presence of these agglomerates can be explained by Van-der-Waals interactions between the particles [37]. Figure 5b shows the particle size distribution corresponding to the microrod length for the $Ca_8NaBi(PO_4)_6F_2$:$0.2Nd^{3+}$ sample. A relatively broad size distribution is observed. The average size of the microcrystals determined by the linear intersection method is about 2.1 μm for the $Ca_8NaBi(PO_4)_6F_2$:$0.2Nd^{3+}$ sample.

The composition of the prepared samples was assessed using EDS line scan analysis and elemental mapping. Figure 6a displays a typical EDS spectrum for the $Ca_8NaBi(PO_4)_6F_2$:$0.2Nd^{3+}$ sample, while Fig. 6b presents the corresponding elemental maps. In the case of the undoped material, the EDS analysis reveals the presence of Ca, Na, Bi, P, and O [32]. However, for the Nd^{3+}-doped sample, the EDS spectrum clearly confirms the presence of Nd, as indicated by the characteristic lines. The mapping of Nd and Bi suggests that the dopant is evenly distributed throughout the host matrix. These EDS studies support the successful synthesis of the $Ca_8NaBi(PO_4)_6F_2$:xNd^{3+} compounds and verify that Nd^{3+} ions have been incorporated in the host lattice, which aligns with the XRD findings.

4.4 Optical absorption

The RT reflectance spectra for the undoped and doped ($x = 0.2$ Nd) samples are shown in Fig. 7a. The spectrum of the Nd^{3+}-doped sample consists of a broad band corresponding to the charge transfer (CT) from the oxygen ligands to the central phosphate atom inside the PO_4^{3-} group and weaker peaks at longer wavelengths corresponding to electronic $(4f^n)$ transitions of Nd^{3+} ions. The absorption bands centered at 530, 591, 750, and 804 nm are assigned to the transitions $^4I_{9/2} \rightarrow {}^4G_{7/2} + {}^4G_{9/2} + {}^2K_{13/2}$, $^4I_{9/2} \rightarrow {}^4G_{5/2} + {}^4G_{7/2} + {}^2H_{11/2}$, $^4I_{9/2} \rightarrow {}^4F_{7/2} + {}^4S_{3/2}$, and $^4I_{9/2} \rightarrow {}^4F_{5/2}$, respectively [38]. The UV absorption edge for the undoped material is found at 297 nm, while for the doped sample with $x = 0.2$, it is slightly red shifted to 305 nm.

The optical bandgap of a powdered sample can be obtained from the reflectance spectra using the Kubelka–Munk relationship [39], according to which, the absorption coefficient (α) and the scattering coefficient (S) are related to the reflectance (R) by the following relation:

$$F(R) = \frac{(1 - R_\infty)^2}{2R} = \frac{\alpha}{S}, \tag{1}$$

where R_∞ is the Kubelka–Munk (KM) function for reflectance. The photon energy (E) and the absorption coefficient (α) are related by the expression [40]:

$$\alpha E = K(E - E_g)^n, \tag{2}$$

where E_g is the bandgap energy, K is a constant and n indicates the type of transition, being 1/2, 3/2, 2, and 3 for direct allowed, direct forbidden, indirect allowed, and indirect forbidden transitions, respectively. In the case of reflectance spectra, the KM function can be replaced by α for the estimation of the bandgap using Eq. (1). At $E = E_g$, a plot of $(\alpha E)^{1/2}$ vs. E which is known as the Tauc plot, Fig. 7b, results in a straight line with the x-intercept value equal to the bandgap. According to this procedure, the direct allowed optical bandgap of the undoped and doped ($x = 0.2Nd$) samples was estimated to be 3.97 eV and 3.91 eV, respectively.

4.5 Near infrared luminescence

The excitation spectra for $Ca_8NaBi(PO_4)_6F_2$ samples doped with Nd^{3+}, monitored at the most intense emission transition of $^4F_{3/2} \rightarrow {}^4I_{11/2}$ (with a wavelength of 1055 nm), were recorded within the range of 700–1000 nm, as depicted in Fig. 8a. These spectra primarily comprise f-f transitions of the Nd^{3+} ions, moving from the ground state of $^4I_{9/2}$ to various excited states. The positions of the excitation bands, specifically $^4I_{9/2} \rightarrow {}^4F_{7/2} + {}^4S_{3/2}$ and $^4I_{9/2} \rightarrow {}^4F_{5/2}$, align well with the reflectance spectrum measurements. Notably, the Nd^{3+} luminescence of $Ca_8NaBi(PO_4)_6F_2$ can be effectively excited by a commercially available 808 nm AlGaAs laser diode. Furthermore, it was observed that Nd^{3+}-doped $Ca_8NaBi(PO_4)_6F_2$ exhibits a relatively broad excitation bandwidth, spanning 20 nm and centered at 804 nm. This characteristic makes it robust against minor fluctuations in the excitation wavelength, such as those arising from variations in diode temperature.
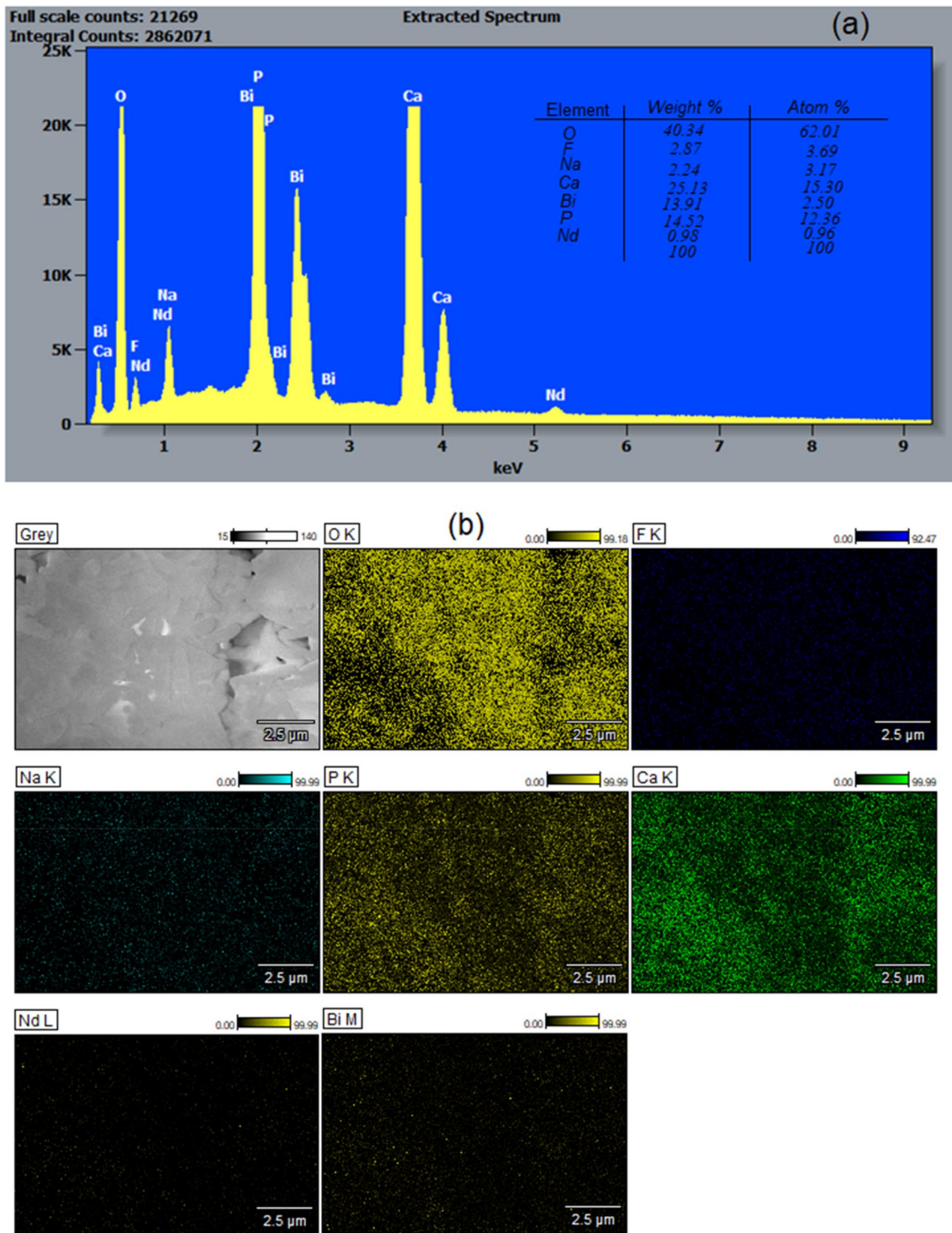
Fig. 6 **a** A typical Energy-Dispersive X-ray (EDX) spectrum of the $Ca_8NaBi(PO_4)_6F_2$:0.2Nd sample; **b** the corresponding SEM image and element maps (O, F, Na, P, Ca, Nd, and Bi)

The near-infrared (NIR) emission spectra of $Ca_8NaBi(PO_4)_6F_2$ fluorapatites doped with Nd^{3+} at various concentrations ($x = 0.05$, 0.1, 0.2, 0.3, 0.4, and 0.5) were recorded under the excitation of an 808 nm laser diode emitting 1.63 W, using identical experimental conditions. Figure 8b shows the emission spectra

Fig. 7 a Reflectance spectra of the host matrix and the $Ca_8NaBi(PO_4)_6F_2$:0.2Nd^{3+} sample and **b** Tauc plot to assess the optical bandgap energy
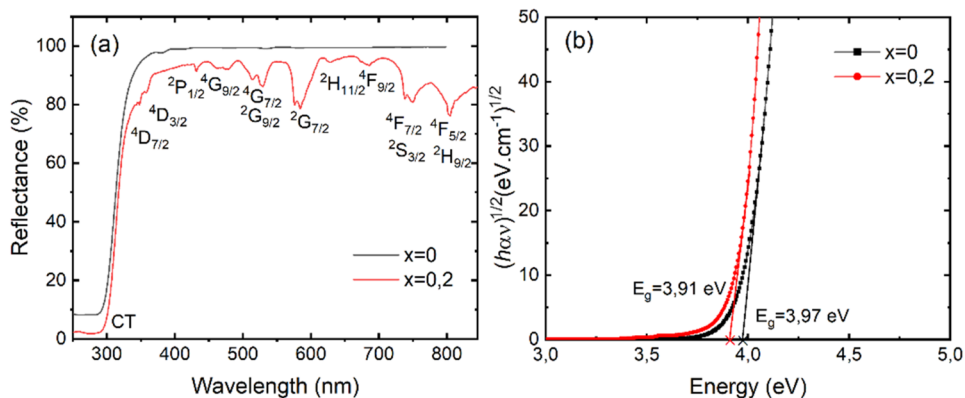

Fig. 8 a Luminescence excitation spectra of the $Ca_8NaBi(PO_4)_6F_2$:xNd^{3+} samples with $x = 0.05$, 0.1, 0.2, 0.3, 0.4, and 0.5 ($\lambda_{lum} = 1055$ nm); **b** shows the emission spectra of $Ca_8NaBi(PO_4)_6F_2$:xNd^{3+} with different Nd^{3+} concentrations, $\lambda_{exc} = 808$ nm; **c** the variation of integral PL intensity of the $^4F_{3/2} \rightarrow {}^4I_{11/2}$ emission band at ~ 1055 nm vs. the Nd^{3+}-doping concentration; **d** analysis of the type of interaction by means of the Dexter equation (x—doping concentration of Nd^{3+}, I—luminescence intensity)
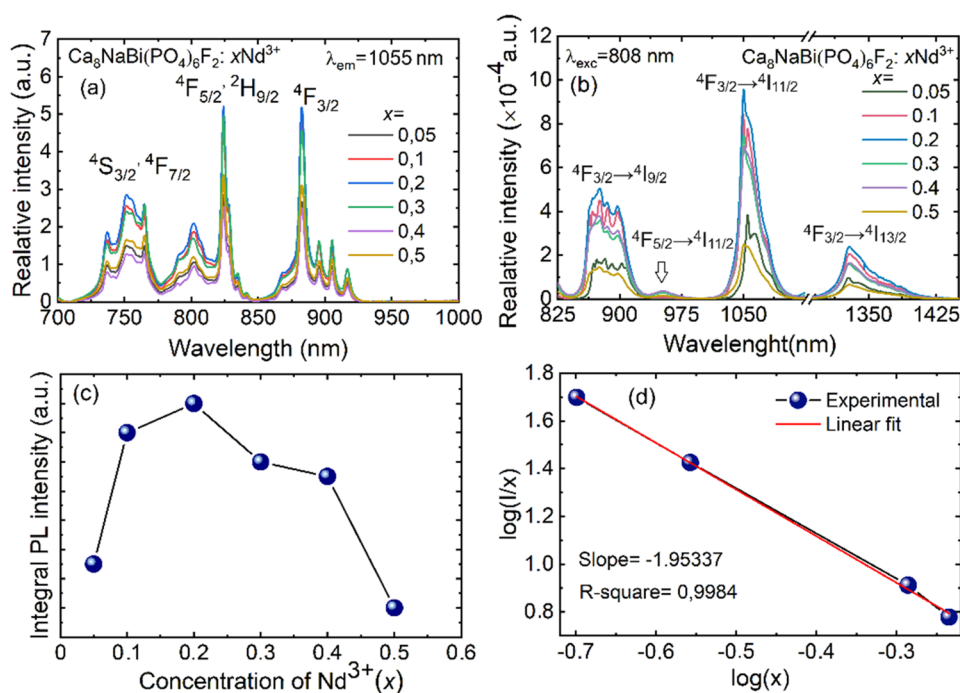
corresponding to different levels of Nd^{3+} ion concentration. These spectra display three distinct emission bands that originate from transitions involving the excited state $^4F_{3/2}$. The most prominent and intense band corresponds to the transition $^4F_{3/2} \rightarrow {}^4I_{11/2}$, peaking at 1055 nm. The emission bands observed in the 865–930 nm and 1330–1400 nm ranges are attributed to the transitions $^4F_{3/2} \rightarrow {}^4I_{9/2}$ and $^4F_{3/2} \rightarrow {}^4I_{13/2}$, respectively. The low-intensity band observed at 957 nm is attributed to the $^4F_{5/2} \rightarrow {}^4I_{11/2}$ transition. The highest luminescence intensity was observed for the $Ca_8NaBi(PO_4)_6F_2$:0.2Nd^{3+} sample.

The emission intensity of $Ca_8NaBi(PO_4)_6F_2$ powders doped with Nd^{3+} ions (with x values ranging from 0.05 to 0.5) is influenced by the dopant ion concentration, while the peak positions and spectral shapes remain constant. Initially, as the doping level increases, the emission intensity rises due to a greater number of emitting centers. However, at higher doping levels, luminescence concentration quenching occurs because electronic excitations migrate to defects and impurities, facilitated by the shorter distances between neighboring dopant ions [41]. In the case of $Ca_8NaBi(PO_4)_6F_2$ powders doped with Nd^{3+}, the emission intensity increases until it reaches its peak at $x = 0.2$Nd. Beyond this concentration, the emission intensity decreases due to concentration quenching, as illustrated in Fig. 8c. This quenching phenomenon can be explained

by two factors: (i) enhanced resonance between the activators as doping concentration increases, leading to the excitation energy reaching quenching centers, and (ii) activators forming pairs that act as quenching centers [42]. For Nd^{3+} ions, a cross-relaxation process depopulating the emitting $^4F_{3/2}$ level occurs: $^4F_{3/2} + {}^4I_{9/2} \rightarrow {}^4I_{15/2}$. Blasse et al. introduced the concept of the critical distance Rc to describe concentration quenching [43]:

$$R_C = \left(\frac{3V}{4\pi\chi CZ}\right)^{\frac{1}{3}}, \tag{3}$$

where Z is the number of substitutable sites for Nd^{3+} for each unit cell; V is the volume of the unit cell; and χ_c is the critical concentration of Nd^{3+}. For $Ca_8NaBi(PO_4)_6F_2{:}0.2Nd^{3+}$, with $Z = 1$, $V = 526.15$ Å^3 (from the XRD data) and $\chi_c = 0.2$ (from the luminescence studies), the resulting R_c is 17.1 Å.

The dominant interaction mechanism can be determined using the equation:

$$\frac{I}{x} = K\left[1 + \beta x^{\left(\frac{\theta}{3}\right)}\right] - 1, \tag{4}$$

where K and β are constants, I denotes the integral luminescence intensity, x is the concentration of the activator ion, and $\theta = 3$, 6, 8, and 10 stand for the nearest-neighbor, dipole–dipole (d–d), dipole–quadrupole (d–q), and quadrupole–quadrupole (q-q) interactions, respectively [30]. Equation (5) can be rewritten as follows:

$$\log\left(\frac{I}{x}\right) = A - \frac{\theta}{3}\log(x), \quad A = \log(k) - \log(\beta). \tag{5}$$

By utilizing luminescence data for x values greater than or equal to 0.2Nd, a logarithmic plot of $\log(I/x)$ versus $\log(x)$ was generated and fitted, resulting in a value of $\theta = 5.86 \pm 0.12$, as displayed in Fig. 8d. This analysis specifically focused on the $^4F_{3/2} \rightarrow {}^4I_{11/2}$ transition of Nd^{3+} ions. The obtained θ value, which is approximately 6, indicates a predominance of the d–d exchange mechanism.

4.6 Luminescence lifetime

Figure 9 shows the photoluminescence decay curves of the $Ca_8NaBi(PO_4)_6F_2{:}xNd$ samples. The excitation and emission wavelengths were 808 nm and 1055 nm, respectively. The decay curves obtained were well fitted by a double-exponential decay function:
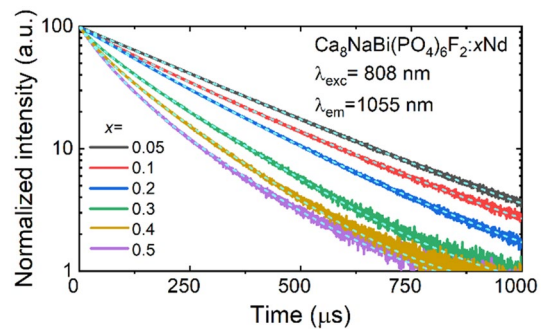
Fig. 9 Luminescence decay curves for the $^4F_{3/2}$ state of Nd^{3+} ions in the $Ca_8NaBi(PO_4)_6F_2{:}xNd$ phosphors with $x = 0.05$, 0.1, 0.2, 0.3, 0.4, and 0.5; $\lambda_{lum} = 1055$ nm and $\lambda_{exc} = 808$ nm; dashed lines are the exponential fit

$$I(t) = A_1 \times \exp\left(-\frac{t}{\tau_1}\right) + A_2 \times \exp\left(-\frac{t}{\tau_2}\right), \tag{6}$$

where A_1 and A_2 are the fitting parameters and τ_1 and τ_2 are the fluorescence decay times, and the average decay time (τ_{av}) was obtained using the following expression:

$$\tau_{av} = \frac{A_1\tau_1^2 + A_2\tau_2^2}{A_1\tau_1 + A_2\tau_2}. \tag{7}$$

The average decay time decreased from 294.4 µs for the sample with the lowest doping level $x = 0.05Nd^{3+}$ to 151.4 µs for the sample with $x = 0.5Nd^{3+}$. The lifetime shortening can be explained in terms of enhancement of the probability of non-radiative interactions between the dopants with shortening the average distance between them. The match of the entire decay curves to the double-exponential function finds explanation within the framework of the Inokuti-Hirayama model [44], particularly evident under conditions where the concentration of Nd^{3+} ions attain relatively high levels. This circumstance prompts an increase in resonant energy transfer among equivalent Nd centers, consequently necessitating the adoption of the double-exponential model for an adequate fit of the luminescence decay curve. This correlation highlights the complex interplay of factors such as ion concentration and resonant energy transfer dynamics, which eventually determine the choice of fitting models to accurately describe luminescence behavior.

4.7 Optical temperature sensing

The temperature-dependent luminescence spectra of $Ca_8NaBi(PO_4)_6F_2$ microrods doped with 0.2% Nd^{3+} were examined within the temperature range of 303 to 403 K, with a 10 K interval, while being excited at 808 nm. The changes in luminescence intensity due to temperature variations were observed for the three most prominent emission peaks of Nd^{3+} ions, occurring at 872, 957, and 1055 nm. This allowed for a comparison of the emission intensity between these three emission bands: two falling within the first biological window (I-BW) range, corresponding to the $^4F_{3/2} \rightarrow {}^4I_{9/2}$ transition at 872 nm (referred to as P2) and $^4F_{5/2} \rightarrow {}^4I_{11/2}$ (P3) transition at 957 nm. The other emission line is within the second biological window (II-BW) range, associated with the $^4F_{3/2} \rightarrow {}^4I_{11/2}$ transition located at 1055 nm (referred to as P1), as illustrated in Fig. 10a. The thermal coupling between the $^4F_{5/2}$ and $^4F_{3/2}$ levels of Nd^{3+} is well recognized and has been the focus of extensive studies aimed at temperature detection, but to our knowledge, this specific pair of transitions ($^4F_{3/2} \rightarrow {}^4I_{11/2}$ /$^4F_{5/2} \rightarrow {}^4I_{11/2}$) has never been pointed out as a possible FIR scheme. As the temperature rises, it is evident in the normalized emission spectra (normalized to the maximum intensity at P1) that the emission bands associated with the
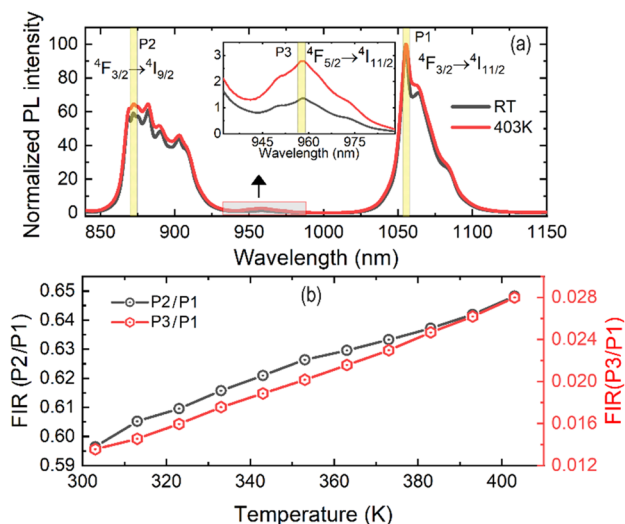

Fig. 10 Thermometry performance characterizations: **a** Normalized photoluminescence emission spectra of the $Ca_8NaBi(PO_4)_6F_2$:0.2Nd^{3+} microrods measured at room temperature (303 K) and 403 K upon 808 nm laser excitation; **b** Plot of FIRs P2/P1 and P3/P1 as a function of temperature (303–403 K); P1 at 1055 nm, P2 at 872 nm, and P3 at 957 nm
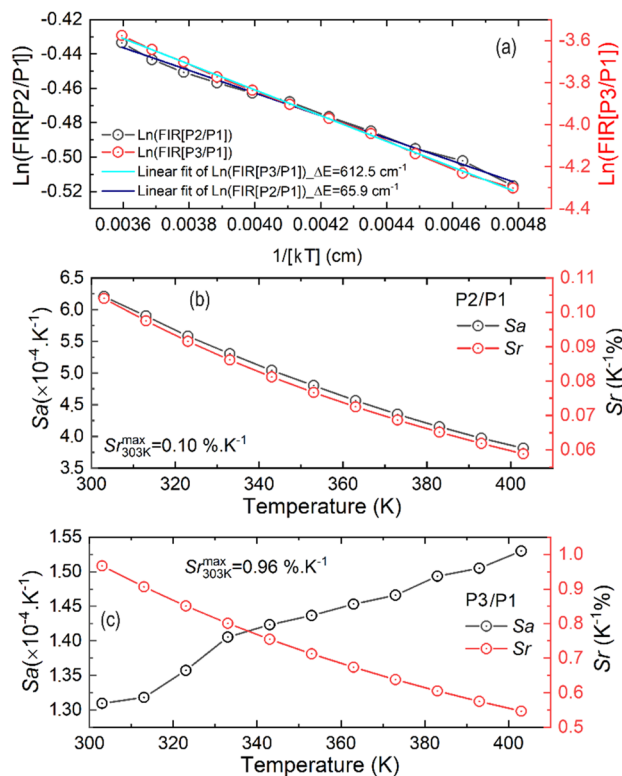

Fig. 11 Thermometry performance characterizations: **a** linear fitting of Ln(FIR) as function of 1/[kT]; Variation of the relative sensitivity (Sr) and the absolute sensitivity (Sa) as function of the temperature (303–403 K): **b** from the FIR P2/P1; **c** from the FIR P3/P1; P1 at 1055 nm, P2 at 872 nm, and P3 at 957 nm

$^4F_{3/2} \rightarrow {}^4I_{9/2}$ (P2) and $^4F_{5/2} \rightarrow {}^4I_{11/2}$ transitions gradually intensify. It should be emphasized that discerning the intricate Stark structure of the transitions $^4F_{3/2} \rightarrow {}^4I_{9/2}$, $^4F_{3/2} \rightarrow {}^4I_{11/2}$, and $^4F_{5/2} \rightarrow {}^4I_{11/2}$ in the measured luminescence spectra is quite challenging, hindering their applicability in single-band luminescence thermometry. Consequently, a thorough investigation into the systematic temperature dependence of the ratios P2/P1 and P3/P1 has been conducted. The FIR can be described by the Boltzmann thermal equilibrium equation:

$$FIR = \frac{P_{i=2,3}}{P1} = C.\exp\left(\frac{-\Delta E}{kT}\right), \qquad (8)$$

where the symbol "P_i" represents the intensity of the emission peak at a specific wavelength, "T" denotes the absolute temperature, "k" stands for the Boltzmann constant, "ΔE" represents the energy difference between the two emissions, and "C" is a constant used in fitting. During the experiments, it was

observed that the ratio of intensities between P2 and P1 in the investigated microrods increased by approximately 9.5% as the temperature increased from 303 to 403 K, as shown in Fig. 10b. In contrast, for the ratio P3/P1, there was a 42% increase at 403 K compared to the value calculated at 303 K. The experimental data presented in Fig. 11a were effectively fitted using this equation, yielding a value of $\Delta E = 65.92$ cm^{-1}, obtained for the FIR P2/P1 and for the ratio P3/P1, the energy gap much higher to be around 612.5 cm^{-1}. The large value of the energy gaps obtained from the FIR P3/P1 curve suggests that large sensitivity can be achieved using this temperature-dependent intensity ratio.

To explore the feasibility of the as-prepared $Ca_8NaBi(PO_4)_6F_2$:Nd^{3+} microrods for luminescence thermometry, it is critical to evaluate the sensitivity of the thermometer. For such single emitting center, it can be defined in absolute terms, or absolute sensitivity Sa:

$$Sa = \left| \frac{dFIR}{dT} \right| = FIR \times \frac{\Delta E}{kT^2}. \tag{9}$$

And in relative terms as it is known by relative thermal sensitivity (Sr) which is considered as an important indicator of the reliability of the measurement. The Sr parameter is described as the rate of the FIR change with temperature, expressed as follows:

$$Sr = \frac{1}{FIR} \times \left| \frac{dFIR}{dT} \right| \times 100\% = \frac{\Delta E}{kT^2} \times 100\%. \tag{10}$$

To compare the performance of distinct thermometers, irrespectively of their nature or the material employed, the relative thermal sensitivity (Sr) should be adopted [45]. The calculated values of Sr and Sa sensitivities within the temperature range of 303 to 403 K from the two FIRs are graphically represented in Fig. 11b and c. It is evident that as the temperature increases, the relative sensitivity shows a declining pattern. The Sr and Sa values at 303 K were compared with those of several standard Nd^{3+}-based luminescent thermometers, and the findings are provided in Table 3. The calculated Sr value for $Ca_8NaBi(PO_4)_6F_2$:Nd^{3+} at 303 K from the FIR P2/P1 is estimated to be 0.10% per degree Kelvin, which is quite consistent with the majority of Nd^{3+}-doped temperature sensors that rely on thermally coupled of the $^4F_{3/2}$ excited state. On the other hand, the calculated thermal sensitivity derived from the second FIR, P3/P1, was significantly higher, 0.96%.K^{-1} at 303 K. This aligns with the thermal sensitivities reported for other luminescent nanothermometers, which operate based on a FIR scheme incorporating transitions from both excited states, $^4F_{5/2}$ and $^4F_{3/2}$. Absolute sensitivity stands out as a crucial metric for exclusively assessing the performance of nanothermometers of the same material nature and tested under the same conditions. This parameter is strictly related to the experimental setup used and the sample characteristics [46]. The absolute sensitivity derived from the P2/P1 ratio reached its maximum value at 303 K, with a notable magnitude of around 6.24×10^{-4}.K^{-1}. As the temperature rises beyond this point, there is a notable drop in this sensitivity. Conversely, if we consider the P3/P1 ratio, absolute sensitivity behaves

Table 3 Comparison of the temperature-sensing performance of different hosts doped with Nd^{3+} ions

Material	λ_{exc} (nm)	Transitions	Temperature range (K)	$Sa(10^{-4}\ K^{-1})$ at 303 K	Sr (%.K^{-1}) at 303 K	Ref
$Y_3Al_5O_{12}$	808	$^4F_{3/2} \rightarrow ^4I_{9/2}$	298–333	–	0.14	[26]
$NaYF_4$	808	$^4F_{3/2} \rightarrow ^4I_{9/2}$	273–423	8.50	0.13	[22]
$KGd(WO_4)_2$	808	$^4F_{3/2} \rightarrow ^4I_{11/2}$	298–333	–	0.16	[48]
LaF_3	808	$^4F_{3/2} \rightarrow ^4I_{9/2}$	283–333	–	0.10	[49]
$BiVO_4$	750	$^4F_{3/2} \rightarrow ^4I_{9/2}$	298–573	–	0.14	[28]
$LiBaPO_4$	800	$^4F_{3/2} \rightarrow ^4I_{9/2}$	294–423	–	0.08	[47]
	532	$^4F_{3/2} \rightarrow ^4I_{9/2}$	294–423	–	0.09	[47]
Bi_2SiO_5	590	$^4F_{5/2} \rightarrow ^4I_{9/2}/^4F_{3/2} \rightarrow ^4I_{9/2}$	280–700	–	1.34	[50]
$Bi_4Si_3O_{12}$	590	$^4F_{5/2} \rightarrow ^4I_{9/2}/^4F_{3/2} \rightarrow ^4I_{9/2}$	280–700	2.30	1.25	[50]
$LiBaPO_4$	800	$^4F_{3/2} \rightarrow ^4I_{9/2}/^4F_{5/2} \rightarrow ^4I_{11/2}$	294–423	–	1.14	[47]
$Ca_8NaBi(PO_4)_6F_2$	808	$^4F_{3/2} \rightarrow ^4I_{11/2}/^4F_{3/2} \rightarrow ^4I_{9/2}$	303–403	6.24	0.10	This work
	808	$^4F_{3/2} \rightarrow ^4I_{11/2}/^4F_{5/2} \rightarrow ^4I_{11/2}$	303–403	1.31	0.96	

distinctly, showing an upward trend in tandem with temperature increases. At 403 K, it reaches its highest level, with a value of $1.53 \times 10^{-4}.K^{-1}$. Through our assessment of the Sr metrics, we have observed that FIR scheme relying on thermal interactions among the excited states $^4F_{5/2}$ and $^4F_{3/2}$ have demonstrated the most impressive outcomes. In contrast, sensors based on Stark sub-levels have exhibited lower relative sensitivity values, particularly within the physiological temperature range [47]. The difference can be clarified by the energy difference (ΔE) between the sets of energy levels employed in FIR calculation. Specifically, the energy gap between the Stark sub-levels of $^4F_{3/2}$ is narrower than the gap between the levels $^4F_{5/2}$ and $^4F_{3/2}$. Consequently, sensors employing the latter pairs of energy levels achieve higher relative sensitivity [47].

In order to evaluate the consistency and reliability of the thermometric correlation, an investigation was conducted on the luminescence intensity ratio P2/P1. This analysis encompassed the examination of spectra obtained during both the heating phase at 403 K and the cooling phase at 303 K cycles. The findings, depicted in Fig. 12a, unveil a remarkable level of temperature measurement reproducibility exceeding 98.5%, with the maximum detected variation standing at 1.5%. In addition, The FIR P3/P1 also exhibited the same degree of variation. These results underscore the robustness and consistency of the thermometric

correlation, affirming its utility in temperature measurement applications. To provide a more comprehensive characterization of the thermometric capabilities of the $Ca_8NaBi(PO_4)_6F_2$:Nd^{3+} microrods, the temperature resolution was also determined. This parameter holds significant importance for a micro/nanothermometer since it defines the smallest temperature variation that can be accurately detected under real operational conditions:

$$\delta T = \frac{\Delta FIR}{FIR} \times \frac{1}{Sr}, \quad (11)$$

where $\Delta FIR/FIR$ presents the relative uncertainty, which is determined to be 1.5% in this study, measured by observing the maximum fluctuation of FIR during four heating and cooling cycles. As depicted in Fig. 12b, the temperature resolution, denoted as δT, deduced from the intensity ratio P2/P1 exhibits a clear ascending pattern, gradually increasing from 0.144 K at 303 K to 0.254 K at 403 K. In contrast, δT derived from the intensity ratio P3/P1 manifests notably lower values, measured to be 0.027 K specifically at the maximum temperature 403 K and < 0.016 K at 303 K. It is worth noting that portable detectors typically require a temperature uncertainty of less than 0.5 K ($\delta T < 0.5$ K) at 300 K [51]. Therefore, further optimization of our $Ca_8NaBi(PO_4)_6F_2$:Nd^{3+} microrods holds the potential to yield more efficient and cost-effective temperature sensors suitable for a wide range of applications.

5 Conclusion

In summary, Nd^{3+}-doped $Ca_8NaBi(PO_4)_6F_2$ phosphors have been successfully synthesized by a modified Pechini process. The XRD results reveal that the studied phosphor crystalizes in the hexagonal apatite phase. The morphology analysis by SEM demonstrates the formation of rod-shaped $Ca_8NaBi(PO_4)_6F_2$:Nd^{3+} particles with an average size of approximately 1.5 µm. These microrods can generate intense NIR emissions in the first and second biological windows under excitation at 808 nm by a laser diode. A comprehensive analysis of the temperature-dependent photoluminescence spectra of $Ca_8NaBi(PO_4)_6F_2$:Nd^{3+} microrods revealed that the luminescent radiometric thermal sensing potential can be achieved based on the intensity ratio of three well spectrally separated peaks of three different emission lines at 1055 nm ($^4F_{3/2} \rightarrow {}^4I_{11/2}$ transition), 872 nm ($^4F_{3/2} \rightarrow {}^4I_{9/2}$ transition), and 957 ($^4F_{5/2} \rightarrow {}^4I_{11/2}$ transition).
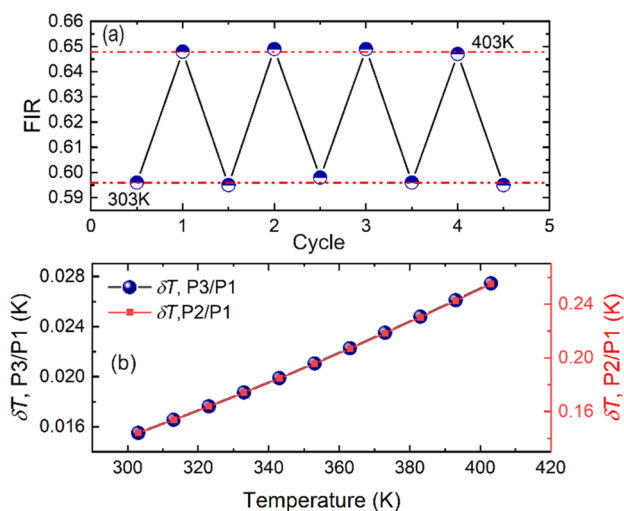

Fig. 12 Thermometry performance characterizations: **a** Reversibility of temperature dependence of the luminescence intensity ratio; **b** Variation of temperature uncertainty (δT) as a function of temperature (303–403 K)

The FIR associated to the thermal coupling between $^4F_{5/2}$ and $^4F_{3/2}$ levels provided the highest relative sensitivity, $0.96\%.K^{-1}$ with an excellent thermal resolution (< 0.016 K at 303 K), and good reproducibility ($> 98.5\%$). The findings obtained in this study provide compelling evidence of the potential efficacy of $Ca_8NaBi(PO_4)_6F_2{:}Nd^{3+}$ micro-rods as sensitive micro-thermometers for accurately measuring and monitoring temperature variations, hereby showcasing their utility as a tool in various thermal sensing applications.

Author contributions

Abir Douzi: Investigation, Methodology, Writing—Original Draft; Sami Slimi: Investigation, Methodology, Conceptualization—Original Draft; Pavel Loiko: Investigation, Review & Editing; Victor Llamas: Investigation; Josep María Serres: Investigation; Rosa Maria Solé: Review & Editing; Magdalena Aguiló: Resources; Francesc Díaz: Resources; Ezzedine Ben Salem: Review & Editing, Supervision; Xavier Mateos: Investigation, Review & Editing, Supervision. Every author provided feedback on earlier drafts of the manuscript, and all authors have reviewed and given their approval for the final version of the manuscript.

Funding

Data availability

The data that support this study are available from the corresponding author upon reasonable request.

Declarations

Conflict of interest We confirm that we do not have any financial or personal affiliations with individuals or organizations that could potentially exert undue influence on our work. There are no professional or personal interests, of any sort, in any product, service, or company that could be interpreted as impacting the stance presented in, or the evaluation of, the manuscript titled, "Temperature sensing by means of a near-infrared luminescent $Ca_8NaBi(PO_4)_6F_2{:}Nd^{3+}$ fluorapatite phosphor."

Ethical approval We hereby assert that this manuscript represents our own original work and has not been published elsewhere or is currently under review by any other publication. The listed authors have thoroughly reviewed the content and have given their approval for the submission of this manuscript to the Journal of Materials Science: Materials in Electronics. We confirm the absence of any personal or financial conflicts of interest. Furthermore, if our article is accepted, we commit to seeking the publisher's consent before publishing it in any other form or language elsewhere.

References

1. B. Liu, C. Li, P. Yang, Z. Hou, J. Lin, Adv. Mater. **29**, 1605434 (2017)

2. E. Hemmer, P. Acosta-Mora, J. Méndez-Ramos, S. Fischer, J. Mater. Chem. B **5**, 4365 (2017)

3. X.D. Wang, O.S. Wolfbeis, R.J. Meier, Chem. Soc. Rev. **42**, 7834 (2013)

4. M. Runowski, P. Woz, S. Lis, V. Lavín, I.R. Martín, M. Runowski, P. Woz, S. Lis, V. Lavín, I.R. Martín, Adv. Mater. Technol. **5**, 1901091 (2020)

5. D. Jaque, F. Vetrone, Nanoscale **4**, 4301 (2012)

6. I.K. van Ravenhorst, R.G. Geitenbeek, M.J. van der Eerden, J. van Tijn Omme, H.H. Peréz Garza, F. Meirer, A. Meijerink, B.M. Weckhuysen, ChemCatChem **11**, 5505 (2019)

7. M. Aldén, A. Omrane, M. Richter, G. Särner, Prog. Energy Combust. Sci. **37**, 422 (2011)

8. J. Brübach, C. Pflitsch, A. Dreizler, B. Atakan, Prog. Energy Combust. Sci. **39**, 37 (2013)

9. M.R. Cates, D.L. Beshears, S.W. Allison, C.M. Simmons, Rev. Sci. Instrum. **68**, 2412 (1997)

10. P. Kolodner, J.A. Tyson, Appl. Phys. Lett. **40**, 782 (1982)

11. K.A. Wickersheim, M.H. Sun, J. Microw. Power Electromagn. Energy **22**, 85 (1987)

12. R.N. Lawson, L.L. Alt, Can. Med. Assoc. J. **92**, 255 (1965)

13. M. Runowski, A. Shyichuk, A. Tymiński, T. Grzyb, V. Lavín, S. Lis, A.C.S. Appl, Mater. Interfaces **10**, 17269 (2018)

14. S. Wang, S. Westcott, W. Chen, J. Phys. Chem. B **106**, 11203 (2002)

15. S. Zhou, X. Li, X. Wei, C. Duan, M. Yin, Sens. Actuators B Chem. **231**, 641 (2016)

16. I.E. Kolesnikov, E.V. Golyeva, A.A. Kalinichev, M.A. Kurochkin, E. Lähderanta, M.D. Mikhailov, Sens. Actuators B Chem. **243**, 338 (2017)

17. Z. Boruc, M. Kaczkan, B. Fetlinski, S. Turczynski, M. Malinowski, Opt. Lett. **37**, 5214 (2012)

18. O.A. Savchuk, J.J. Carvajal, M.C. Pujol, E.W. Barrera, J. Massons, M. Aguilo, F. Diaz, J. Phys. Chem. C **119**, 18546 (2015)

19. S.F. León-Luis, V. Monteseguro, U.R. Rodríguez-Mendoza, M. Rathaiah, V. Venkatramu, A.D. Lozano-Gorrín, R. Valiente, A. Muñoz, V. Lavín, RSC Adv. **4**, 57691 (2014)

20. A.F. Pereira, K.U. Kumar, W.F. Silva, W.Q. Santos, D. Jaque, C. Jacinto, Sens. Actuators B Chem. **213**, 65 (2015)

21. I.E. Kolesnikov, E.V. Golyeva, E. Lähderanta, A.V. Kurochkin, M.D. Mikhailov, J. Nanoparticle Res. (2016). https://doi.org/10.1007/s11051-016-3675-8

22. D. Wawrzynczyk, A. Bednarkiewicz, M. Nyk, W. Strek, M. Samoc, Nanoscale **4**, 6959 (2012)

23. S. Balabhadra, M.L. Debasu, C.D.S. Brites, L.A.O. Nunes, O.L. Malta, J. Rocha, M. Bettinelli, L.D. Carlos, Nanoscale **7**, 17261 (2015)

24. U. Rocha, K.U. Kumar, C. Jacinto, I. Villa, F. Sanz-Rodríguez, M. de la Del Carmen Iglesias Cruz, A. Juarranz, E. Carrasco, F.C.J.M. Van Veggel, E. Bovero, J.G. Solé, D. Jaque, Small **10**, 1141 (2014)

25. Z.F. Yu, J.P. Shi, J.L. Li, P.H. Li, H.W. Zhang, J. Mater. Chem. B **6**, 1238 (2018)

26. A. Benayas, B. Del Rosal, A. Pérez-Delgado, K. Santacruz-Gómez, D. Jaque, G.A. Hirata, F. Vetrone, Adv. Opt. Mater. **3**, 687 (2015)

27. I.E. Kolesnikov, A.A. Kalinichev, M.A. Kurochkin, E.V. Golyeva, E.Y. Kolesnikov, A.V. Kurochkin, E. Lähderanta, M.D. Mikhailov, Sci. Rep. **7**, 1 (2017)

28. P.M. Gschwend, F.H.L. Starsich, R.C. Keitel, S.E. Pratsinis, Chem. Commun. **55**, 7147 (2019)

29. Y. Shang, S. Hao, J. Liu, M. Tan, N. Wang, C. Yang, G. Chen, Nanomaterials **5**, 218 (2014)

30. S. Slimi, P. Loiko, K. Bogdanov, A. Volokitina, R.M. Solé, M. Aguiló, F. Díaz, E. Ben Salem, X. Mateos, J. Alloys Compd. **896**, 163109 (2022)

31. F. Mirjalili, S. Manafi, F. Lotfi, Ceram. Int. **46**, 21256 (2020)

32. S. Slimi, P. Loiko, A. Volokitina, K. Bogdanov, R.M. Solé, M. Aguiló, F. Díaz, E. Ben Salem, X. Mateos, J. Lumin. **241**, 118523 (2022)

33. R. D. Shannon and IUCr, Urn:Issn:0567–7394 **32**, 751 (1976).

34. Y.J. Han, S. Wang, H. Liu, L. Shi, A.J. Song, X.L. Lu, J.Y. Wei, Z.Y. Mao, D.J. Wang, Z.F. Mu, Z.W. Zhang, J. Alloys Compd. **844**, 156070 (2020)

35. L. Pajchel, L. Borkowski, Materials (Basel). **14**, 6936 (2021)

36. J. Latocha, M. Wojasiński, O. Janowska, U. Chojnacka, S. Gierlotka, T. Ciach, P. Sobieszuk, AIChE J. **1**, 17897 (2022)

37. T. Kobori, S. Iwamoto, K. Takeyasu, T. Ohtani, Biopolymers **85**, 392 (2007)

38. P. Loiko, A. Pavlyuk, S. Slimi, R.M. Solé, E. Ben Salem, E. Dunina, A. Kornienko, P. Camy, U. Griebner, V. Petrov, F. Díaz, M. Aguiló, X. Mateos, J. Lumin. (2021). https://doi.org/10.1016/j.jlumin.2014.11.010

39. S.K. Sharma, S. Som, R. Jain, A.K. Kunti, J. Lumin. **159**, 317 (2015)

40. D.K. Singh, J. Manam, Electron. Mater. Lett. **13**, 292 (2017)

41. P. Dorenbos, R. Visser, R. Dool, J. Andriessen, C.W.E. Van Eijk, J. Phys. Condens. Matter **4**, 5281 (1992)

42. P. Du, J.S. Yu, J. Lumin. **179**, 451 (2016)

43. P. You, G. Yin, X. Chen, B. Yue, Z. Huang, X. Liao, Y. Yao, Opt. Mater. (Amst). **33**, 1808 (2011)

44. M. Inokuti, F. Hirayama, J. Chem. Phys. **43**, 1978–1989 (1965)

45. C.D.S. Brites, S. Balabhadra, L.D. Carlos, Advanced Optical Materials **7**, 1801239 (2019)

46. A. Nexha, J.J. Carvajal, M.C. Pujol, F. Díaz, M. Aguiló, Nanoscale **13**, 7913–7987 (2021)

47. A.S. Laia, D.A. Hora, M.V. Marcos, Y. Xing, J.J. Rodrigues, G.S. Maciel, M.A.R.C. Alencar, Chem. Eng. J. (2020). https://doi.org/10.1016/j.cej.2020.125742

48. O. Savchuk, J.J. Carvajal, L.G. De La Cruz, P. Haro-González, M. Aguiló, F. Díaz, J. Mater. Chem. C **4**, 7397 (2016)

49. U. Rocha, C. Da Jacinto Silva, W. Ferreira Silva, I. Guedes, A. Benayas, L. Martínez Maestro, M. Acosta Elias, E. Bovero, F.C.J.M. van Veggel, J.A. García Solé, D. Jaque, ACS Nano **7**, 1188 (2013)

50. D. Chen, Y. Liang, S. Miao, J. Bi, K. Sun, J. Lumin. **234**, 117967 (2021)

51. C.D.S. Brites, A. Millán, L.D. Carlos, Handb. Phys. Chem. Rare Earths **49**, 339 (2016)